ChemComm

COMMUNICATION

View Article Online
View Journal

Cite this: DOI: 10.1039/d0cc08273b

Received 21st December 2020,
Accepted 26th January 2021

DOI: 10.1039/d0cc08273b

rsc.li/chemcomm

A conjugated tetracarboxylate anode for stable and sustainable Na-ion batteries†

Kaiqiang Qin, [a] Kathryn Holguin, [a] Motahareh Mohammadiroudbari[a] and Chao Luo *[ab]

A conjugated tetracarboxylate, 1,2,4,5-benzenetetracarboxylate sodium salt ($Na_4C_{10}H_2O_8$), was designed and synthesized as an anode material in Na-ion batteries (NIBs). This organic compound shows low redox potentials (~0.65 V), long cycle life (1000 cycles), and fast charging capability (up to 2 A g^{-1}), demonstrating a promising organic anode for stable and sustainable NIBs.

The ever-growing demands for energy and environmental sustainability have stimulated the development of low-cost and environmentally benign energy storage devices. However, conventional Li-ion batteries (LIBs) cannot satisfy these demands because of the high cost, limited availability and uneven distribution of lithium resources. Considerable research efforts have been devoted to searching for cost-effective and sustainable alternatives to LIBs. Among them, Na-ion batteries (NIBs) stand out because of the low cost, abundance, and high sustainability of sodium resources, as well as the similar electrochemistry of NIBs to LIBs.[1,2] To date, a rich variety of inorganic cathode and anode materials have been developed for NIBs, including sodium transition metal oxides, sodium transition metal phosphates, metal sulfides, hard carbons, *etc.*[3–6] Nevertheless, the larger ion size of Na^+ than Li^+ and more complicated Na^+ storage electrochemistry are detrimental to the performance of inorganic materials in NIBs.[7] The electrochemical performance of NIBs based on inorganic electrode materials is still not comparable with that of LIBs in terms of the specific capacity and cycle life. To overcome this challenge, developing novel high-capacity and long-lifetime electrode materials is critical.

Organic electrode materials (OEMs) with the advantages of low cost, abundance, lightweight, high sustainability, flexible structural tunability, and abundant structural diversity show great promise for high-performance NIBs.[8–12] Due to the universal electrochemical properties of OEMs in rechargeable batteries, their high performances in LIBs are extended to NIBs.[13–16] To date, a large number of OEMs based on carbonyl group, imine group, azo group, free radical, and so forth, have been used to reversibly store Na^+.[17–21] The low molecular weights and tunable structures of OEMs enable high-capacity NIBs. However, there are still two major challenges in organic NIBs: (1) low electronic conductivity results in slow reaction kinetics; (2) high solubility in the organic electrolyte leads to fast capacity decay.[22–24] To circumvent these challenges, a large amount of conductive carbon is added to organic electrodes to enhance the electronic conductivity. In addition, the salt formation and polymerization of small organic compounds are effective approaches to reducing the solubility of OEMs and improving their long-term cycling stability.[25–27] Therefore, high-performance OEMs can be achieved for stable and sustainable NIBs by rational structural design.

In this work, the salt formation method was adopted to synthesize three conjugated sodium carboxylates as anode materials for NIBs. The molecular structure of these conjugated carboxylates with two carboxylate groups (benzene-1, 3-dicarboxylate sodium salt, $Na_2C_8H_4O_4$), three carboxylate groups (1,2,3-benzenetricarboxylate sodium salt, $Na_3C_9H_3O_6$), and four carboxylate groups (1,2,4,5-benzenetetracarboxylate sodium salt, $Na_4C_{10}H_2O_8$) are shown in Scheme 1a–c. $Na_2C_8H_4O_4$ and $Na_3C_9H_3O_6$ with carboxylate groups at the *ortho* and *meta* positions are employed as control samples. We proved that $Na_2C_8H_4O_4$ with two carboxylate groups at the *meta* positions is electrochemically inactive, while $Na_3C_9H_3O_6$ with three carboxylate groups at the *ortho* and *meta* positions, respectively, is electrochemically active but suffers from poor cycle life, especially at high current densities. $Na_4C_{10}H_2O_8$ with four carboxylate groups at *ortho*, *meta*, and *para* positions exhibits the best electrochemical performance in terms of high capacity, long cycle life, and fast charging capability. The two carboxylate groups at the *para* positions of the benzene ring are

[a] *Department of Chemistry and Biochemistry, George Mason University, Fairfax, VA, 22030, USA. E-mail: cluo@gmu.edu*
[b] *Quantum Science & Engineering Center, George Mason University, Fairfax, VA, 22030, USA*

† Electronic supplementary information (ESI) available. See DOI: 10.1039/d0cc08273b

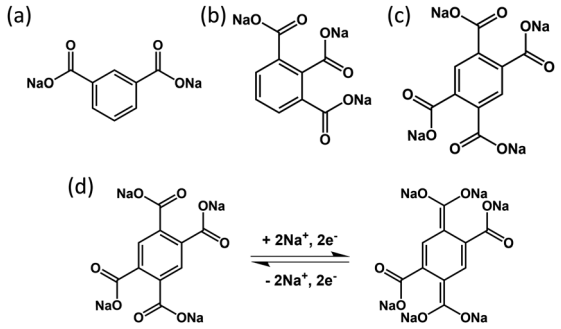

Scheme 1 The molecular structure of three sodium carboxylates: (a) $Na_2C_8H_4O_4$, (b) $Na_3C_9H_3O_6$, and (c) $Na_4C_{10}H_2O_8$; (d) the sodiation/de-sodiation mechanism of $Na_4C_{10}H_2O_8$.

electrochemically active centers to reversibly react with Na-ions and electrons (Scheme 1d). The superior electrochemical performance of $Na_4C_{10}H_2O_8$ is further exploited by cyclic voltammetry (CV) at various scan rates, galvanostatic intermittent titration technique (GITT), and electrochemical impedance spectroscopy (EIS) to understand the fast reaction kinetics in NIBs. Fourier-transform infrared spectroscopy (FTIR) and X-ray powder diffraction (XRD) were also used to study the molecular and crystalline structure evolution of $Na_4C_{10}H_2O_8$ upon cycling. The results confirm that the capacitive reaction kinetics, small overpotential, low interfacial resistance and stable crystalline/molecular structure upon cycling contribute to the exceptional performance of $Na_4C_{10}H_2O_8$ in NIBs.

The structures of $Na_4C_{10}H_2O_8$ and the two control samples, $Na_2C_8H_4O_4$ and $Na_3C_9H_3O_6$, were characterized by XRD, FTIR, proton nuclear magnetic resonance (^{1}H NMR), Carbon-13 nuclear magnetic resonance (^{13}C NMR) and scanning electron microscopy (SEM). As shown in Fig. 1a and Fig. S1a, S2a (ESI†), all the three materials show crystalline structures. The sharp and intense absorption peaks at $\sim$1580 cm^{-1} and $\sim$1390 cm^{-1} in FTIR spectra (Fig. 1b and Fig. S1b, S2b, ESI†) represent the asymmetric and symmetric stretching vibrations of carboxylate groups in these aromatic compounds, respectively.[28] The molecular structures of these conjugated carboxylates are further studied by ^{1}H NMR and ^{13}C NMR with D_2O as the solvent. In Fig. 1c, the sharp peak at $\sim$7.85 ppm represents the two protons attached to the benzene ring of $Na_4C_{10}H_2O_8$, which have the same chemical environment and are located at the same chemical shift in ^{1}H NMR. In addition, there are three peaks at 128 ppm, 136 ppm, and 173 ppm in ^{13}C NMR (Fig. 1d), representing the sp^2 carbons in the benzene ring bonded with protons, the sp^2 carbons in the benzene ring bonded with carboxylate groups, and the sp^2 carbons in the carboxylate groups, respectively. The ^{1}H NMR and ^{13}C NMR spectra of $Na_2C_8H_4O_4$ and $Na_3C_9H_3O_6$ in Fig. S1c, d and S2c, d (ESI†) also confirm their molecular structures. The morphology of these conjugated carboxylates was investigated by SEM. As shown in Fig. 1e and f, $Na_4C_{10}H_2O_8$ consists of micro-sized particles (1–5 μm) with numerous nanorods aggregated together, while $Na_2C_8H_4O_4$ and $Na_3C_9H_3O_6$ consist of irregular shaped micro-sized particles (Fig. S1e and S2e, ESI†). These results confirm the chemical structure and morphology of the conjugated carboxylates.

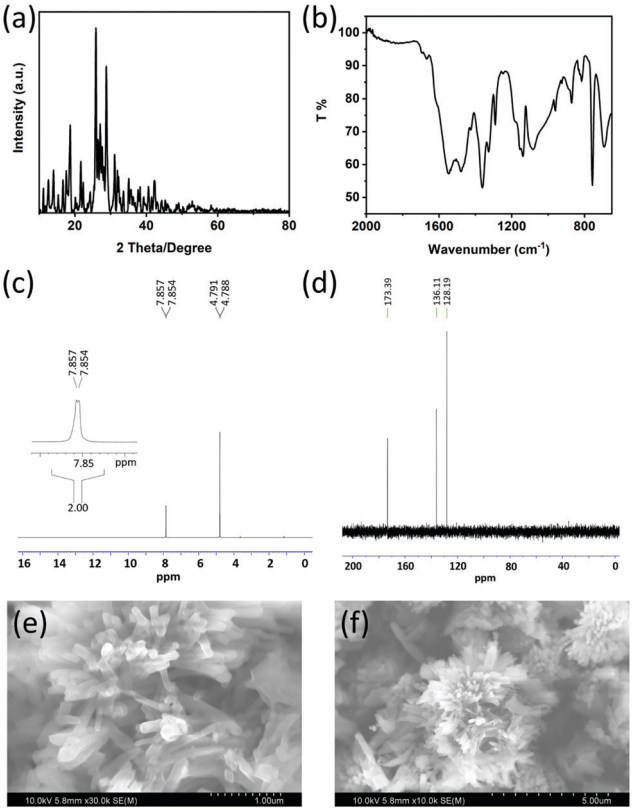

Fig. 1 Material characterizations for $Na_4C_{10}H_2O_8$. (a) XRD pattern, (b) FTIR spectrum, (c) ^{1}H NMR spectrum, and (d) ^{13}C NMR spectrum. SEM images with scale bars of (e) 1 μm and (f) 5 μm.

To investigate the electrochemical performance in NIBs, these conjugated carboxylates are used as active materials to couple with the sodium metal. As shown in Fig. S3a (ESI†), the galvanostatic charge/discharge curves of $Na_2C_8H_4O_4$ do not exhibit any plateau after the first discharge and are similar to that of carbon black (Fig. S4, ESI†). Moreover, its reversible capacity upon cycling is less than 15 mA h g^{-1} (Fig. S3b, ESI†), which is attributed to the capacity of carbon black. This result demonstrates that $Na_2C_8H_4O_4$ with two carboxylate groups at *meta* positions is electrochemically inactive in NIBs. To further exploit the electrochemical behaviors of conjugated carboxylate anodes, a carboxylate group is added between the two carboxylate groups in $Na_2C_8H_4O_4$ to provide $Na_3C_9H_3O_6$, which shows one pair of redox plateaus centered at 0.5 V in Fig. S5a (ESI†). At a low current density of 20 mA g^{-1}, $Na_3C_9H_3O_6$ delivers a de-sodiation capacity of 186.7 mA h g^{-1} in the first cycle. In cyclic voltammograms (Fig. S5b, ESI†), a sharp cathodic peak at 0.1 V and a broad peak at 0.65 V are observed from the 1st to 4th cycles, corresponding to the redox plateaus centered at 0.5 V in the charge/discharge curves. When cycling at 20 mA g^{-1}, a reversible capacity of 131 mA h g^{-1} is retained after 30 cycles (Fig. S5c, ESI†), demonstrating moderate cyclic stability. However, the reversible capacity of $Na_3C_9H_3O_6$ at 500 mA g^{-1} is remarkably decreased to 38.7 mA h g^{-1}, and a very low capacity of 18.1 mA h g^{-1} is retained after 400 cycles (Fig. S5d, ESI†), demonstrating poor cycle life at a high current density. In the rate capability result (Fig. S5e, ESI†),

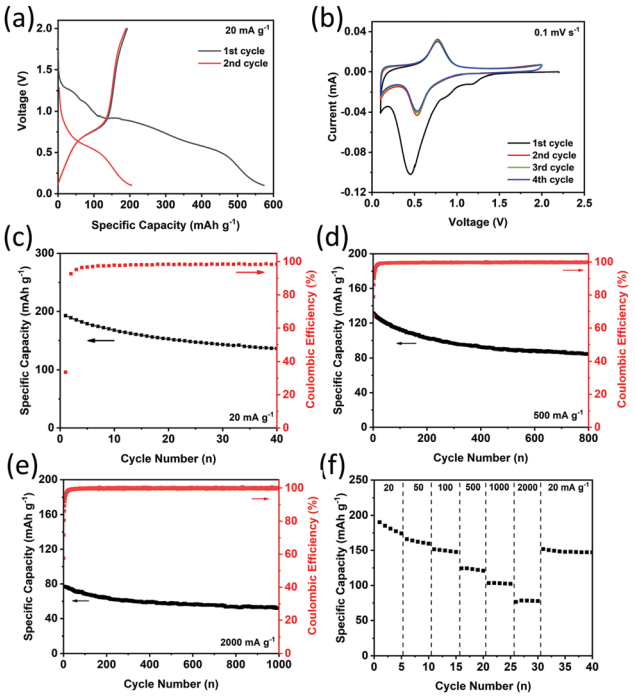

Fig. 2 Electrochemical performance of $Na_4C_{10}H_2O_8$ in NIBs. (a) Galvanostatic charge–discharge curves; (b) cyclic voltammograms at 0.1 mV s^{-1}; de-sodiation capacity and coulombic efficiency *versus* cycle number at the current density of (c) 20 mA g^{-1}, (d) 500 mA g^{-1}, (e) 2000 mA g^{-1}; (f) rate performance at various current densities.

the specific capacity of $Na_3C_9H_3O_6$ is quickly reduced from ~180 mA h g^{-1} to below 50 mA h g^{-1} after the current density increases from 20 mA g^{-1} to 500 mA g^{-1}. When the current density further increases to 1 A g^{-1} and 2 A g^{-1}, the specific capacity drops to ~21 mA h g^{-1} and ~7 mA h g^{-1}, respectively, demonstrating sluggish reaction kinetics.

To further improve the electrochemical performance of conjugated carboxylate anodes, we add two carboxylate groups to $Na_2C_8H_4O_4$ to provide $Na_4C_{10}H_2O_8$. As shown in Fig. 2a, $Na_4C_{10}H_2O_8$ exhibits one pair of redox plateaus centered at 0.65 V with a reversible capacity of 192.7 mA h g^{-1}. Compared to $Na_3C_9H_3O_6$, the reaction potential increase of $Na_4C_{10}H_2O_8$ is ascribed to the addition of an extra carboxylate group, which is an electron-withdrawing functional group and changes the electronic structure and molecular orbital energy level of the conjugated carboxylate. In cyclic voltammograms (Fig. 2b), one pair of cathodic and anodic peaks at ~0.5 V and ~0.75 V are observed, corresponding to redox plateaus centered at 0.65 V (Fig. 2a). In the long-term cycling tests (Fig. 2c–e), reversible capacities of 136.1 mA h g^{-1} at 20 mA g^{-1}, 84 mA h g^{-1} at 500 mA g^{-1}, and 51.4 mA h g^{-1} at 2 A g^{-1} are retained after 40 cycles, 800 cycles, and 1000 cycles, respectively, demonstrating exceptional cycling stability. The coulombic efficiency upon long-term cycling is close to 100%. The rate capability of $Na_4C_{10}H_2O_8$ is measured from 20 mA g^{-1} to 2 A g^{-1}. As shown in Fig. 2f, the reversible capacities of 103 mA h g^{-1} and 78 mA h g^{-1} can be retained, even though the current density increases from 20 mA g^{-1} to 1 A g^{-1} and 2 A g^{-1}. After the current density reduces back to 20 mA g^{-1}, a reversible capacity of 149.5 mA h g^{-1} can still be retained, demonstrating robust reaction kinetics. The exceptional electrochemical performance of $Na_4C_{10}H_2O_8$ renders it a promising organic anode material in stable and sustainable NIBs.

To further understand the electrochemical behaviors, CV, GITT, and EIS were employed to study the reaction kinetics of $Na_4C_{10}H_2O_8$ in NIBs. As shown in Fig. 3a, the $Na_4C_{10}H_2O_8$ anode was cycled at various scan rates from 0.1 mV s^{-1} to 2 mV s^{-1}. The peak intensity increases with elevated scan rates. The cathodic peak slightly shifts to a lower potential, while the anodic peak slightly shifts to a higher potential, due to the enhanced polarization. The linear fit of the natural logarithm relationship of scan rate and the peak current is displayed in Fig. 3b. Since the slope (b) values of cathodic and anodic peaks are 0.7269 and 0.7043, respectively, the reaction kinetics of $Na_4C_{10}H_2O_8$ anode exhibits a partial capacitive behavior, which contributes to the high-rate capability.[29] In Fig. 3c, the equilibrium potentials obtained from GITT show that the charge/discharge equilibrium potentials of $Na_4C_{10}H_2O_8$ are centered at 0.7 V/0.6 V, and the overpotentials are only 35 mV and 40 mV at the charge and discharge plateau regions, respectively. The small overpotential validates the high-rate capability of the $Na_4C_{10}H_2O_8$ anode. To further study the reaction kinetics, EIS analysis is carried out to analyze the interfacial resistance of the $Na_4C_{10}H_2O_8$ anode, which is represented by the depressed semi-circle in Fig. 3d. The interfacial impedance of the fresh $Na_4C_{10}H_2O_8$ anode is ~270 ohm, which gradually enhances to ~300 ohm after 10 cycles and stabilizes at ~300 ohm after 50 cycles. The stable interfacial impedance from the 10th cycle to the 50th cycle demonstrates the stable solid electrolyte interphase layer on the $Na_4C_{10}H_2O_8$ anode upon cycling, which contributes to the stable cycle life of $Na_4C_{10}H_2O_8$ anode in NIBs. The CV, GITT, and EIS results confirm the good reaction

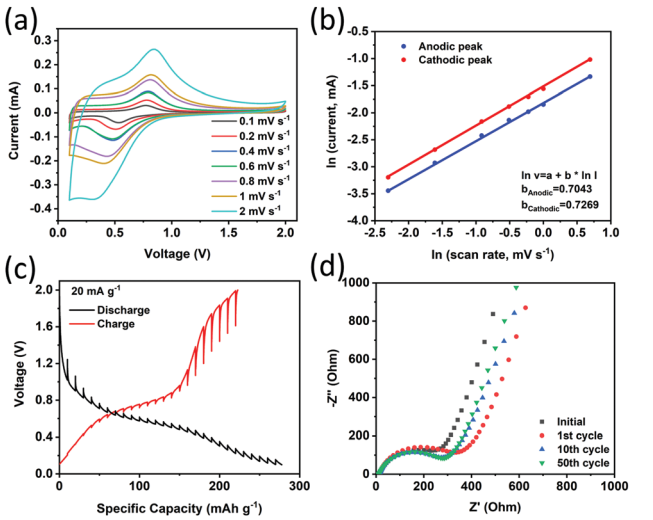

Fig. 3 Reaction kinetics of $Na_4C_{10}H_2O_8$ in NIBs. (a) Cyclic voltammograms at various scan rates; (b) the ln relationship of peak current and scan rate; (c) potential response during GITT measurements; (d) impedance analysis before and after charge/discharge.

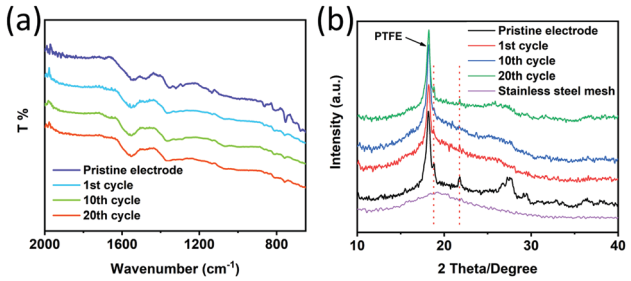

Fig. 4 (a) FTIR spectra and (b) XRD patterns of $Na_4C_{10}H_2O_8$ anodes before and after cycling.

kinetics and a stable interface layer of the $Na_4C_{10}H_2O_8$ anode in NIBs.

In addition to the reaction kinetics, FTIR and XRD were used to exploit the molecular and crystalline structure change upon cycling. As shown in Fig. 4a, the FTIR spectra do not change from the pristine electrode to the 20th cycle, demonstrating the stable molecular structure of $Na_4C_{10}H_2O_8$ upon cycling. In XRD tests, thick electrodes were prepared by using polytetrafluoroethylene (PTFE) as a binder, which shows a strong and sharp peak at 18.4 degree in Fig. 4b. The peak for PTFE does not change upon cycling, while the broad peaks from 25 degree to 30 degree for $Na_4C_{10}H_2O_8$ disappear after the first cycle, but the peaks at 18.7 degree and 21.7 degree remain from the first cycle to the 20th cycle, demonstrating that a crystalline structure change occurs in the first cycle and the newly formed crystalline structure retains afterwards. These results further confirm the stable structure of $Na_4C_{10}H_2O_8$ upon cycling, demonstrating that the conjugated carboxylate anode is promising for stable and sustainable NIBs.

In conclusion, three conjugated carboxylate anode materials were designed and synthesized for NIBs. The conjugated carboxylate ($Na_2C_8H_4O_4$) with two carboxylate groups at the *meta* positions are electrochemically inactive, while $Na_3C_9H_3O_6$ and $Na_4C_{10}H_2O_8$ are electrochemically active. However, with three carboxylate groups next to each other, $Na_3C_9H_3O_6$ suffers from sluggish reaction kinetics and poor cycle life at a high current density. $Na_4C_{10}H_2O_8$ with four carboxylate groups at the *ortho*, *meta*, and *para* positions shows the best electrochemical performance in terms of high capacity, long cycle life, and fast charging capability. CV, GITT, and EIS results confirm the fast reaction kinetics and stable interfacial resistance, while FTIR and XRD results demonstrate the stable molecular and crystalline structure upon cycling. Therefore, this work confirms that the conjugated tetracarboxylate is a promising anode material for stable and sustainable NIBs.

This work was supported by the US National Science Foundation Award No. 2000102 and the George Mason University, College of Science Postdoctoral Fellowship. The authors also acknowledge the support from the George Mason University Quantum Science & Engineering Center.

Conflicts of interest

There are no conflicts to declare.

Notes and references

1 H. Pan, Y. S. Hu and L. Chen, *Energy Environ. Sci.*, 2013, **6**, 2338–2360.
2 V. Palomares, P. Serras, I. Villaluenga, K. B. Hueso, J. Carretero-González and T. Rojo, *Energy Environ. Sci.*, 2012, **5**, 5884.
3 N. Yabuuchi, K. Kubota, M. Dahbi and S. Komaba, *Chem. Rev.*, 2014, **114**, 11636–11682.
4 Y. Fang, Q. Liu, L. Xiao, Y. Rong, Y. Liu, Z. Chen, X. Ai, Y. Cao, H. Yang, J. Xie, C. Sun, X. Zhang, B. Aoun, X. Xing, X. Xiao and Y. Ren, *Chemistry*, 2018, **4**, 1167–1180.
5 Y. Fang, D. Luan, Y. Chen, S. Gao and X. W. Lou, *Angew. Chem., Int. Ed.*, 2020, **59**, 7178–7183.
6 X. Dou, I. Hasa, D. Saurel, C. Vaalma, L. Wu, D. Buchholz, D. Bresser, S. Komaba and S. Passerini, *Mater. Today*, 2019, **23**, 87–104.
7 P. K. Nayak, L. Yang, W. Brehm and P. Adelhelm, *Angew. Chem., Int. Ed.*, 2018, **57**, 102–120.
8 J. J. Shea and C. Luo, *ACS Appl. Mater. Interfaces*, 2020, **12**, 5361–5380.
9 R. Rajagopalan, Y. Tang, C. Jia, X. Ji and H. Wang, *Energy Environ. Sci.*, 2020, **13**, 1568–1592.
10 K. Qin, J. Huang, K. Holguin and C. Luo, *Energy Environ. Sci.*, 2020, **13**, 3950–3992.
11 X. Yin, S. Sarkar, S. Shi, Q. A. Huang, H. Zhao, L. Yan, Y. Zhao and J. Zhang, *Adv. Funct. Mater.*, 2020, **30**, 1908445.
12 R. Shi, L. Liu, Y. Lu, C. Wang, Y. Li, L. Li, Z. Yan and J. Chen, *Nat. Commun.*, 2020, **11**, 178.
13 P. Poizot, J. Gaubicher, S. Renault, L. Dubois, Y. Liang and Y. Yao, *Chem. Rev.*, 2020, **120**, 6490–6557.
14 M. Mao, C. Luo, T. P. Pollard, S. Hou, T. Gao, X. Fan, C. Cui, J. Yue, Y. Tong, G. Yang, T. Deng, M. Zhang, J. Ma, L. Suo, O. Borodin and C. Wang, *Angew. Chem., Int.*, 2019, **58**, 17820–17826.
15 A. V. Desai, R. E. Morris and A. R. Armstrong, *ChemSusChem*, 2020, **13**, 4866–4884.
16 C. Luo, J. J. Shea and J. Huang, *J. Power Sources*, 2020, **453**, 227904.
17 L. Y. Wang, C. Ma, X. Wei, B. Chang, K. X. Wang and J. S. Chen, *J. Mater. Chem. A*, 2020, **8**, 8469–8475.
18 K. Sakaushi, E. Hosono, G. Nickerl, T. Gemming, H. Zhou, S. Kaskel and J. Eckert, *Nat. Commun.*, 2013, **4**, 1485.
19 C. Luo, O. Borodin, X. Ji, S. Hou, K. J. Gaskell, X. Fan, J. Chen, T. Deng, R. Wang, J. Jiang and C. Wang, *Proc. Natl. Acad. Sci. U. S. A.*, 2018, **115**, 2004–2009.
20 C. Luo, G. L. Xu, X. Ji, S. Hou, L. Chen, F. Wang, J. Jiang, Z. Chen, Y. Ren, K. Amine and C. Wang, *Angew. Chem., Int. Ed.*, 2018, **57**, 2879–2883.
21 Y. Xu, M. Zhou and Y. Lei, *Mater. Today*, 2018, **21**, 60–78.
22 S. Lee, J. Hong and K. Kang, *Adv. Energy Mater.*, 2020, **10**, 2001445.
23 S. Wu, W. Wang, M. Li, L. Cao, F. Lyu, M. Yang, Z. Wang, Y. Shi, B. Nan, S. Yu, Z. Sun, Y. Liu and Z. Lu, *Nat. Commun.*, 2016, **7**, 13318.
24 C. Luo, X. Fan, Z. Ma, T. Gao and C. Wang, *Chemistry*, 2017, **3**, 1050–1062.
25 Y. Lu, Q. Zhang, L. Li, Z. Niu and J. Chen, *Chemistry*, 2018, **4**, 2786–2813.
26 Q. Zhao, J. Wang, Y. Lu, Y. Li, G. Liang and J. Chen, *Angew. Chem.*, 2016, **128**, 12716–12720.
27 S. Gu, S. Wu, L. Cao, M. Li, N. Qin, J. Zhu, Z. Wang, Y. Li, Z. Li, J. Chen and Z. Lu, *J. Am. Chem. Soc.*, 2019, **141**, 9623–9628.
28 F. Génin, F. Quilès and A. Burneau, *Phys. Chem. Chem. Phys.*, 2001, **3**, 932–942.
29 V. Augustyn, J. Come, M. A. Lowe, J. W. Kim, P. L. Taberna, S. H. Tolbert, H. D. Abruña, P. Simon and B. Dunn, *Nat. Mater.*, 2013, **12**, 518–522.

